

## Dynamic response of functionally gradient austenitic-ferritic steel composite panels under thermo-mechanical loadings

S. Isavand<sup>1</sup>, M. Bodaghi<sup>\*1</sup>, M. Shakeri<sup>1</sup> and J. Aghazadeh Mohandesi<sup>2</sup>

<sup>1</sup> *Thermoelasticity Center of Excellence, Department of Mechanical Engineering, Amirkabir University of Technology, Tehran, Iran*

<sup>2</sup> *Department of Mining and Metallurgical Engineering, Amirkabir University of Technology, Tehran, Iran*

*(Received February 13, 2014, Revised May 02, 2014, Accepted May 09, 2014)*

**Abstract.** In this paper, the dynamic response of functionally gradient steel (FGS) composite cylindrical panels in steady-state thermal environments subjected to impulsive loads is investigated for the first time. FGSs composed of graded ferritic and austenitic regions together with bainite and martensite intermediate layers are analyzed. Thermo-mechanical material properties of FGS composites are predicted according to the microhardness profile of FGS composites and approximated with appropriate functions. Based on the three-dimensional theory of thermo-elasticity, the governing equations of motion are derived in spatial and time domains. These equations are solved using the hybrid Fourier series expansion-Galerkin finite element method-Newmark approach for simply supported boundary conditions. The present solution is then applied to the thermo-elastic dynamic analysis of cylindrical panels with three different arrangements of material compositions of FGSs including  $\alpha\beta\gamma M\gamma$ ,  $\alpha\beta\gamma\beta\alpha$  and  $\gamma\beta\alpha\beta\gamma$  composites. Benchmark results on the displacement and stress time-histories of FGS cylindrical panels in thermal environments under various pulse loads are presented and discussed in detail. Due to the absence of similar results in the specialized literature, this paper is likely to fill a gap in the state of the art of this problem, and provide pertinent results that are instrumental in the design of FGS structures under time-dependent mechanical loadings.

**Keywords:** functionally gradient steels; cylindrical panel; 3-D thermo-elasticity solution; thermo-elastic dynamic response

### 1. Introduction

Functionally gradient materials (FGMs) are a new kind of composites in which the material properties vary smoothly and continuously as a function of position in one or more specific direction (Suresh and Mortensen 1998). This is achieved by gradually changing the volume fraction of the constituent materials. FGMs are usually made from a mixture of ceramic and metal or combinations of different metals using powder metallurgy techniques. FGMs may possess a number of advantages such as high resistance to temperature gradients, significant reduction in interlaminar and thermal stresses, high wear resistance, etc. (Suresh and Mortensen 1998).

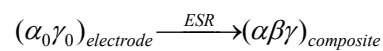
In the last two decades, numerous research works have been dedicated to the static and

---

\*Corresponding author, Ph.D. Candidate, E-mail: [m.bodaghi@aut.ac.ir](mailto:m.bodaghi@aut.ac.ir)

dynamic analysis of preliminary structural elements such as beams, plates, shells and panels made of conventional metal-ceramic FGMs. For instance, Santos *et al.* (2009) presented a semi-analytical finite element model to study bending and free vibrations of functionally graded (FG) cylindrical shells based on the three-dimensional (3-D) theory of elasticity. The material properties were graded in the thickness direction according to a power-law distribution of the volume fraction of the constituents. Zhao *et al.* (2009) investigated static response and free vibration of FG cylindrical panels using the element-free  $kp$ -Ritz method. They employed Sander's first-order shear deformation theory (FSDT) to describe the displacement field of the FG shell. Cinefra *et al.* (2010) presented a thermo-mechanical analysis of simply supported FG panels. Refined shell theories were used to account for grading material variation in the thickness direction. Sofiyev (2010) introduced an analytical study on the dynamic behavior of infinitely-long, FG cylindrical shells subjected to combined action of the axial tension, constant internal compressive load and ring-shaped compressive pressures with constant velocity. Foroutan *et al.* (2011) developed static analysis of axisymmetric FG cylinders subjected to internal and external pressure using a mesh-free method. Moving least square shape functions were used for approximation of displacement field in the weak form of equilibrium equation and essential boundary conditions were imposed by transformation method. Based on the 3-D theory of elasticity, free vibration of FG cylindrical shells embedded in piezoelectric layers was investigated by Alibeigloo *et al.* (2012) using the state space approach and differential quadrature method (DQM). Large amplitude vibration behavior of FG cylindrical shells embedded in a large outer elastic medium and in thermal environments was analyzed by Shen (2012). The governing equations of motion were derived based on the higher-order shear deformation theory and solved by a two-step perturbation technique. Kamarian *et al.* (2013) studied free vibration characteristics of simply supported FG sandwich rectangular plates resting on elastic foundations based on the 3-D elasticity theory. The material constituents were graded through the thickness according to a three-parameter power-law distribution.

Functionally gradient steels (FGSs) with strength gradient, are a group of functionally graded materials that provide a way of gaining the highest advantages of multi-phase systems containing ferritic, bainitic, austenitic and martensitic phases. For the first time, these materials were produced from plain carbon steel and austenitic stainless steel using electroslag remelting (ESR) process by Aghazadeh Mohandesi and Shahosseini (2005). In electroslag remelting process, by selecting appropriate arrangements and thicknesses of the original ferritic steel ( $\alpha_0$ ) and original austenitic steel ( $\gamma_0$ ) as electrodes, different composites of FGS are obtained with several graded layers consist of ferrite, bainite, austenite and martensite. When the primary electrodes contain two layers of original ferritic steel and original austenitic steel, a bainitic layer appears in the final composite, thereby the final composite contains the ferritic and austenitic graded regions together with the bainitic layer as follows



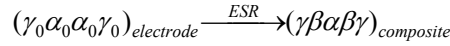
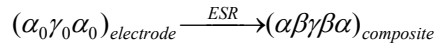
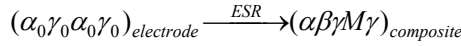
where  $\alpha$ ,  $\gamma$  and  $\beta$  are the ferritic graded region, the austenitic graded region and the bainitic layer in the final composite, respectively.

When primary electrodes consist of two original austenitic steel layers and one original ferritic steel layer in the middle, due to the gathering of alloying elements such as Nickel and Chromium that are diffused from the two austenitic steel layers to the middle ferritic steel layer and decrease in Carbon atoms, the ferrite turns into the martensite. The resulted composite can be written as



where  $\gamma$  and  $M$  are the austenitic graded region and the martensitic layer in the final composite, respectively.

Similarly, when primary electrodes consist of three or four layers of original austenitic steel and original ferritic steel, the following FGSs are produced



Several experimental and numerical research works have been carried out about thermo-mechanical properties of FGSs. Aghazadeh Mohandesi and Shahosseinie (2005) investigated experimentally transformation characteristics of FGSs and obtained microhardness profile of these alloys. Aghazadeh Mohandesi *et al.* (2006) studied the tensile behavior of FGSs, experimentally and numerically. The results reveal that the tensile strength of FGS composites depends on the type and number of layers in the composite and it regards to the tensile behavior of individual layer. Nazari and Aghazadeh Mohandesi (2009, 2010) examined experimentally charpy impact energy of FGSs in both crack divider and crack arrester configurations and modeled them by various methods. The results reveal that the impact energy in the crack divider configuration depends on the type and the volume fraction of the constituent phases of composites. Furthermore, it is found that the notch tip position with respect to bainite or martensite layers affects the impact energy in the crack arrester configuration.

With the introduction of FGSs, it is important to get a comprehensive realization of the behavior of FGS structures for reliable design of these strength gradient structures. Recently, Talebizad *et al.* (2013) presented an axisymmetric thermo-mechanical analysis of FGS cylindrical pressure vessels under static internal pressure with arrangements of  $\gamma M \gamma$  and  $\alpha\beta\gamma$ . Governing equations of equilibrium were derived based on the 2-D elasticity theory and solved using finite element methods. They found that FGS pressure vessels evinced unusual thermo-mechanical behaviors in comparison with conventional metal-ceramic FG structures.

Reviewing the literature on the analysis of FGS structures reveals that there exists only one research paper (Talebizad *et al.* 2013) which has been published on the static analysis of axisymmetric FGS cylindrical pressure vessels under internal pressure. To the best of authors' knowledge, there is no research work on the dynamic analysis of FGS structures in the open literature. This issue motivates us to develop a transient thermo-elastic analysis of cylindrical panels made of FGSs as a practical structural component in thermal environments under pulse loads.

The main objective of the present study is to explore the dynamic response of simply supported FGS cylindrical panels in thermal environments subjected to impulsive loads. Three arrangements of FGS composites including  $\alpha\beta\gamma M \gamma$ ,  $\alpha\beta\gamma\beta\alpha$  and  $\gamma\beta\alpha\beta\gamma$  composites are analyzed. Thermo-mechanical material properties of FGS composites are predicted according to the microhardness profile reported by Aghazadeh Mohandesi and Shahosseinie (2005) and are approximated with appropriate functions. On the basis of the 3-D thermo-elasticity theory, the governing equations of

motion and steady-state heat transfer equation are derived. Utilizing double Fourier series expansion in the axial and circumferential directions, the highly coupled partial differential equations with four independent spatial and time variables are reduced to partial differential equations in radial coordinate and time domains. The Galerkin finite element method is then employed to obtain a solution of the system of equations in radial spatial coordinate. Finally, Newmark-beta scheme is used to treat the time dependency. Due to lack of any data on the thermo-elastic analysis of FGS open panels, static analysis of a conventional metal-ceramic FG panel is performed to verify the accuracy of the present results in comparison with the published data. Finally, a detailed analysis of the influence of different arrangements of material compositions of FGSs on the displacement and stress time-histories of functionally gradient steel cylindrical panels in thermal environments under various impulsive loads is carried out. Due to the absence of similar results in the specialized literature, it is expected that the results of this research will contribute to a better understanding of the dynamic behavior of FGS structures in thermal environments exposed to pulse loads.

## 2. Materials and methods

### 2.1 Material properties of the FGS panel

Consider a finite functionally gradient steel cylindrical panel with length  $L$ , internal radius  $R_{in}$ , external radius  $R_{out}$ , mean radius  $R_m$ , thickness  $h(R_{out}-R_{in})$  and angular span  $\theta_m$  as depicted in Fig. 1. The cylindrical coordinate system  $(r, \theta, z)$  is assumed where  $r, \theta, z$  refer to the radial, circumferential and axial directions of the panel.

It is assumed that the thermo-mechanical material properties of the panel vary across the thickness direction. In the present work, three kinds of functionally gradient steel including  $\alpha\beta\gamma M\gamma$  composite,  $\alpha\beta\gamma\beta\alpha$  composite and  $\gamma\beta\alpha\beta\gamma$  composite are analyzed.

The thermo-mechanical material properties are assumed according to the micro hardness profile reported by Aghazadeh Mohandesi and Shahosseini (2005). Based on the experimental observation, the variation of Poisson ratio ( $\nu$ ) and density ( $\rho$ ) is small and it is assumed to be constant for convenience. Furthermore, since the thickness of bainitic and martensitic layers are small, the thermo-mechanical material properties of these layers are considered to be constant in  $\alpha\beta\gamma M\gamma$ ,  $\alpha\beta\gamma\beta\alpha$  and  $\gamma\beta\alpha\beta\gamma$  composites. Moreover, the thermo-mechanical material properties in the ferritic and outer austenitic regions of  $\alpha\beta\gamma M\gamma$  composite, ferritic regions of  $\alpha\beta\gamma\beta\alpha$  composite and austenitic regions of  $\gamma\beta\alpha\beta\gamma$  composite can be approximated with exponential functions through the thickness direction as

$$E = a_1 e^{a_2 \zeta} \quad (1a)$$

$$k = b_1 e^{b_2 \zeta} \quad (1b)$$

$$\alpha = c_1 e^{c_2 \zeta} \quad (1c)$$

On the other hand, the thermo-mechanical material properties of the centric austenitic region of  $\alpha\beta\gamma M\gamma$  and  $\alpha\beta\gamma\beta\alpha$  composites and ferritic region of  $\gamma\beta\alpha\beta\gamma$  composite are approximated with quadratic polynomial functions through the thickness direction as

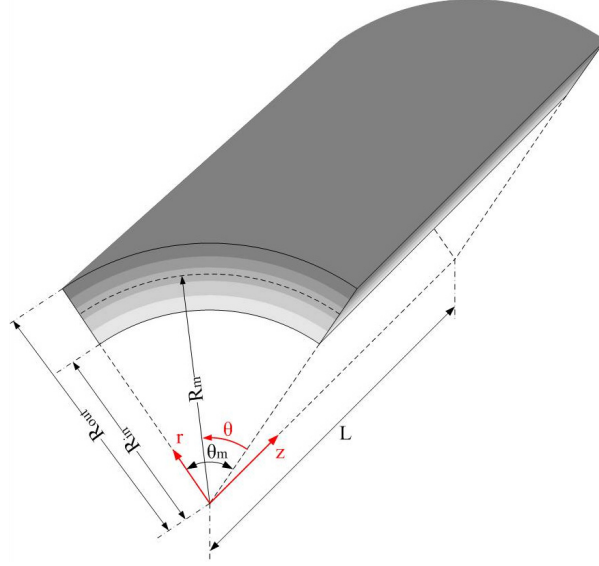


Fig. 1 Geometry and dimensions of the FGS cylindrical panel

$$E = d_1\zeta^2 + d_2\zeta + d_3 \quad (2a)$$

$$k = e_1\zeta^2 + e_2\zeta + e_3 \quad (2b)$$

$$\alpha = f_1\zeta^2 + f_2\zeta + f_3 \quad (2c)$$

where  $E$ ,  $k$  and  $\alpha$  denote Young modulus, thermal conductivity coefficient and coefficient of thermal expansion, respectively. Also,  $a_i$ ,  $b_i$ ,  $c_i$ ,  $d_j$ ,  $e_j$  and  $f_j$  ( $i = 1, 2$  and  $j = 1, 2, 3$ ) are constant and  $\zeta$  is normalized thickness direction defined as  $(r-R_m)/h$ .

## 2.2 Governing equations

In the present analysis, the functionally gradient steel panel is assumed to be made of many sub layers. Each sub layer is considered as an isotropic layer. The thermo-mechanical material properties in each layer are constant and functionally gradient properties are resulted by suitable arrangement of layers in the multilayer panel.

The linear constitutive thermo-elastic equations can be written for each layer as

$$\begin{Bmatrix} \sigma_r \\ \sigma_\theta \\ \sigma_z \\ \tau_{\theta z} \\ \tau_{rz} \\ \tau_{r\theta} \end{Bmatrix} = \begin{bmatrix} C_{11} & C_{12} & C_{13} & 0 & 0 & 0 \\ C_{21} & C_{22} & C_{23} & 0 & 0 & 0 \\ C_{31} & C_{32} & C_{33} & 0 & 0 & 0 \\ 0 & 0 & 0 & C_{44} & 0 & 0 \\ 0 & 0 & 0 & 0 & C_{55} & 0 \\ 0 & 0 & 0 & 0 & 0 & C_{66} \end{bmatrix} \begin{Bmatrix} \varepsilon_r - \alpha_1 T \\ \varepsilon_\theta - \alpha_2 T \\ \varepsilon_z - \alpha_3 T \\ \gamma_{\theta z} \\ \gamma_{rz} \\ \gamma_{r\theta} \end{Bmatrix} \quad (3)$$

where  $\sigma_i/\varepsilon_i$  ( $i = r, \theta, z$ ) are the components of normal stresses/strains, while  $\tau_i/\gamma_i$  ( $i = \theta z, rz, r\theta$ ) denote components of shear stresses/strains. Also,  $C_{ij}$  ( $i, j = 1, 2, 3, 4, 5, 6$ ) and  $\alpha_i$  ( $i = 1, 2, 3$ ) represent elastic constants and coefficients of thermal expansion, respectively. Furthermore,  $T$  is the temperature change from the stress-free reference temperature.

In the absence of body forces, the three-dimensional equations of motion and the steady-state heat conduction equation can be expressed as

$$\begin{aligned} \frac{\partial \sigma_r}{\partial r} + \frac{1}{r} \frac{\partial \tau_{r\theta}}{\partial \theta} + \frac{\partial \tau_{rz}}{\partial z} + \frac{\sigma_r - \sigma_\theta}{r} &= \rho \frac{\partial^2 u_r}{\partial t^2} \\ \frac{\partial \tau_{r\theta}}{\partial r} + \frac{1}{r} \frac{\partial \sigma_\theta}{\partial \theta} + \frac{\partial \tau_{z\theta}}{\partial z} + \frac{2\tau_{r\theta}}{r} &= \rho \frac{\partial^2 u_\theta}{\partial t^2} \\ \frac{\partial \tau_{rz}}{\partial r} + \frac{1}{r} \frac{\partial \tau_{z\theta}}{\partial \theta} + \frac{\partial \sigma_z}{\partial z} + \frac{\tau_{rz}}{r} &= \rho \frac{\partial^2 u_z}{\partial t^2} \\ \frac{1}{r} \frac{\partial r q_r}{\partial r} + \frac{1}{r} \frac{\partial q_\theta}{\partial \theta} + \frac{\partial q_z}{\partial z} &= 0 \end{aligned} \quad (4)$$

where  $q_i$  ( $i = r, \theta, z$ ) are the heat flux components.

The linear strain-displacement relations are given as

$$\begin{aligned} \varepsilon_r &= \frac{\partial u_r}{\partial r}, & \varepsilon_\theta &= \frac{u_r}{r} + \frac{1}{r} \frac{\partial u_\theta}{\partial \theta}, & \varepsilon_z &= \frac{\partial u_z}{\partial z} \\ \gamma_{rz} &= \frac{\partial u_r}{\partial z} + \frac{\partial u_z}{\partial r}, & \gamma_{r\theta} &= \frac{1}{r} \frac{\partial u_r}{\partial \theta} - \frac{u_\theta}{r} + \frac{\partial u_\theta}{\partial r}, & \gamma_{\theta z} &= \frac{1}{r} \frac{\partial u_z}{\partial \theta} + \frac{\partial u_\theta}{\partial z} \end{aligned} \quad (5)$$

where  $u_r$ ,  $u_\theta$  and  $u_z$  are the radial, circumferential and longitudinal displacement components.

The relationships between the components of heat flux and temperature change are

$$q_r = -k_1 \frac{\partial T}{\partial r}, \quad q_\theta = -k_2 \frac{\partial T}{\partial \theta}, \quad q_z = -k_3 \frac{\partial T}{\partial z} \quad (6)$$

where  $k_i$  ( $i = 1, 2, 3$ ) are the thermal conductivity coefficients.

Substituting Eqs. (3), (5), and (6) into Eq. (4), the governing equations of motion and heat conduction for each layer of the FGS cylindrical panel are obtained as

$$\begin{aligned} &\left[ C_{11} \frac{\partial^2}{\partial r^2} + \frac{C_{11}}{r} \frac{\partial}{\partial r} - \left( \frac{C_{22}}{r^2} - \frac{C_{66}}{r^2} \frac{\partial^2}{\partial \theta^2} - C_{55} \frac{\partial^2}{\partial z^2} \right) \right] u_r \\ &+ \left[ \frac{(C_{12} + C_{66})}{r} \frac{\partial^2}{\partial r \partial \theta} - \frac{(C_{22} + C_{66})}{r^2} \frac{\partial}{\partial \theta} \right] u_\theta + \left[ (C_{13} + C_{55}) \frac{\partial^2}{\partial r \partial z} - \frac{(C_{23} - C_{13})}{r} \frac{\partial}{\partial z} \right] u_z \\ &- (C_{11} \alpha_1 + C_{12} \alpha_2 + C_{13} \alpha_3) \frac{\partial T}{\partial r} - \frac{[(C_{11} - C_{12}) \alpha_1 + (C_{12} - C_{22}) \alpha_2 + (C_{13} - C_{23}) \alpha_3]}{r} T = \rho \frac{\partial^2 u_r}{\partial t^2} \end{aligned} \quad (7)$$

↓

$$\begin{aligned}
& \uparrow \\
& \left[ \frac{(C_{12} + C_{66})}{r} \frac{\partial^2}{\partial r \partial \theta} + \frac{(C_{22} + C_{66})}{r^2} \frac{\partial}{\partial \theta} \right] u_r + \left[ C_{66} \frac{\partial^2}{\partial r^2} + \frac{C_{66}}{r} \frac{\partial}{\partial r} - \left( \frac{C_{66}}{r^2} - \frac{C_{22}}{r^2} \frac{\partial^2}{\partial \theta^2} - C_{44} \frac{\partial^2}{\partial z^2} \right) \right] u_\theta \\
& + \left[ \frac{(C_{23} + C_{44})}{r} \frac{\partial^2}{\partial z \partial \theta} \right] u_z - \frac{(C_{12}\alpha_1 + C_{22}\alpha_2 + C_{23}\alpha_3)}{r} \frac{\partial T}{\partial \theta} = \rho \frac{\partial^2 u_\theta}{\partial t^2} \\
& \left[ (C_{13} + C_{55}) \frac{\partial^2}{\partial r \partial z} + \frac{(C_{23} + C_{55})}{r} \frac{\partial}{\partial z} \right] u_r + \left[ \frac{(C_{23} + C_{44})}{r} \frac{\partial^2}{\partial z \partial \theta} \right] u_\theta \\
& + \left[ C_{55} \frac{\partial^2}{\partial r^2} + \frac{C_{55}}{r} \frac{\partial}{\partial r} + \frac{C_{44}}{r^2} \frac{\partial^2}{\partial \theta^2} + C_{33} \frac{\partial^2}{\partial z^2} \right] u_z - (C_{13}\alpha_1 + C_{23}\alpha_2 + C_{33}\alpha_3) \frac{\partial T}{\partial z} = \rho \frac{\partial^2 u_z}{\partial t^2} \\
& k_1 \left( \frac{\partial^2 T}{\partial r^2} + \frac{1}{r} \frac{\partial T}{\partial r} \right) + \frac{k_2}{r^2} \frac{\partial^2 T}{\partial \theta^2} + k_3 \frac{\partial^2 T}{\partial z^2} = 0
\end{aligned} \tag{7}$$

Eq. (7) is four highly coupled partial differential equations in terms of displacements and the temperature change in spatial and time domains. These equations will be solved for the dynamic analysis of FGS cylindrical panels in thermal environments under impulsive loads in the future sections.

### 2.3 Boundary and continuity conditions

It is assumed that the FGS cylindrical panel has simply supported boundary conditions on all four edges and its edges are maintained in the reference temperature. These thermo-mechanical boundary conditions can be written as

$$\begin{aligned}
u_r = u_z = \sigma_\theta = T = 0 & \quad \text{at} \quad \theta = 0, \theta_m \\
u_r = u_\theta = \sigma_z = T = 0 & \quad \text{at} \quad z = 0, L
\end{aligned} \tag{8}$$

Continuity conditions of stresses, displacements and temperature should follow Eq. (9) for the interface between every two adjacent sub layers

$$\begin{aligned}
\sigma_r)_k = \sigma_r)__{k+1}, \quad \tau_{r\theta})_k = \tau_{r\theta})_{k+1}, \quad \tau_{rz})_k = \tau_{rz})_{k+1}, \quad q_r)_k = q_r)__{k+1} \\
u_r)_k = u_r)__{k+1}, \quad u_\theta)_k = u_\theta)__{k+1}, \quad u_z)_k = u_z)__{k+1}, \quad T)_k = T)__{k+1}
\end{aligned} \tag{9}$$

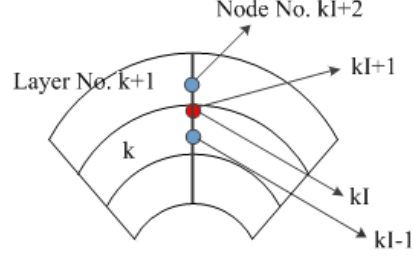
where  $k$  and  $k + 1$  stand for two adjacent layers, see Fig. 2.

The surface conditions at the inner and outer surfaces of the cylindrical panel are given as

$$\begin{aligned}
\sigma_r = q_0(\theta, z, t), \quad \tau_{r\theta} = \tau_{rz} = 0, \quad T = T_{in}(\theta, z) \quad \text{at} \quad r = R_{in} \\
\sigma_r = p_0(\theta, z, t), \quad \tau_{r\theta} = \tau_{rz} = 0, \quad T = T_{out}(\theta, z) \quad \text{at} \quad r = R_{out}
\end{aligned} \tag{10}$$

### 2.4 Solution methodology

The solution of coupled partial differential Eq. (7) in the axial and circumferential directions, satisfying the thermo-mechanical boundary conditions (8), is taken in the following double Fourier

Fig. 2 Two adjacent layers  $k$  and  $k + 1$ 

series forms

$$\begin{aligned}
 u_r &= \sum_{n=1}^{\infty} \sum_{m=1}^{\infty} \varphi_r(r, t) \sin(b_m \theta) \sin(b_n z) \\
 u_\theta &= \sum_{n=1}^{\infty} \sum_{m=1}^{\infty} \varphi_\theta(r, t) \cos(b_m \theta) \sin(b_n z) \\
 u_z &= \sum_{n=1}^{\infty} \sum_{m=1}^{\infty} \varphi_z(r, t) \sin(b_m \theta) \cos(b_n z) \\
 T &= \sum_{n=1}^{\infty} \sum_{m=1}^{\infty} T(r) \sin(b_m \theta) \sin(b_n z)
 \end{aligned} \tag{11}$$

where  $b_m = m\pi/\theta_m$ ,  $b_n = n\pi/L$ , and  $m$  and  $n$  denote the number of half-waves in the  $\theta$  and  $z$  directions, respectively. Moreover, the mechanical and thermal loads may be expanded into the following form

$$p_0(\theta, z, t) = \sum_{n=1}^{\infty} \sum_{m=1}^{\infty} P_0(t) \sin(b_m \theta) \sin(b_n z) \tag{12a}$$

$$q_0(\theta, z, t) = \sum_{n=1}^{\infty} \sum_{m=1}^{\infty} Q_0(t) \sin(b_m \theta) \sin(b_n z)$$

$$T_{in}(\theta, z) = \sum_{n=1}^{\infty} \sum_{m=1}^{\infty} T_{in} \sin(b_m \theta) \sin(b_n z) \tag{12b}$$

$$T_{out}(\theta, z) = \sum_{n=1}^{\infty} \sum_{m=1}^{\infty} T_{out} \sin(b_m \theta) \sin(b_n z)$$

Substituting Eq. (11) into Eq. (7), the partial differential equations with four independent spatial and time variables reduce to partial differential equations with variable coefficients in radial coordinate and time domains as

$$\left[ C_{11} \frac{\partial^2}{\partial r^2} + \frac{C_{11}}{r} \frac{\partial}{\partial r} - \left( \frac{C_{22}}{r^2} + \frac{C_{66}}{r^2} b_m^2 + C_{55} b_n^2 \right) \right] \varphi_r \tag{13}$$

↓

$$\begin{aligned}
& \uparrow \\
& + \left[ -b_m \frac{(C_{12} + C_{66})}{r} \frac{\partial}{\partial r} + b_m \frac{(C_{22} + C_{66})}{r^2} \right] \varphi_\theta + \left[ -b_n (C_{13} + C_{55}) \frac{\partial}{\partial r} + b_n \frac{(C_{23} - C_{13})}{r} \right] \varphi_z \\
& - (C_{11}\alpha_1 + C_{12}\alpha_2 + C_{13}\alpha_3) \frac{dT}{dr} - \frac{[(C_{11} - C_{12})\alpha_1 + (C_{12} - C_{22})\alpha_2 + (C_{13} - C_{23})\alpha_3]T}{r} = \rho \frac{\partial^2 \varphi_r}{\partial t^2} \\
& \left[ b_m \frac{(C_{12} + C_{66})}{r} \frac{\partial}{\partial r} + \frac{(C_{22} + C_{66})}{r^2} b_m \right] \varphi_r + \left[ C_{66} \frac{\partial^2}{\partial r^2} + \frac{C_{66}}{r} \frac{\partial}{\partial r} - \left( \frac{C_{66}}{r^2} + \frac{C_{22}}{r^2} b_m^2 + C_{44} b_n^2 \right) \right] \varphi_\theta \\
& + \left[ \frac{-(C_{23} + C_{44})}{r} b_n b_m \right] \varphi_z - \frac{(C_{12}\alpha_1 + C_{22}\alpha_2 + C_{23}\alpha_3)}{r} b_m T = \rho \frac{\partial^2 \varphi_\theta}{\partial t^2} \\
& \left[ (C_{13} + C_{55}) b_n \frac{\partial}{\partial r} + \frac{(C_{23} + C_{55})}{r} b_n \right] \varphi_r + \left[ -\frac{(C_{23} + C_{44})}{r} b_n b_m \right] \varphi_\theta \\
& + \left[ C_{55} \frac{\partial^2}{\partial r^2} + \frac{C_{55}}{r} \frac{\partial}{\partial r} - \frac{C_{44}}{r^2} b_m^2 - C_{33} b_n^2 \right] \varphi_z - b_n (C_{13}\alpha_1 + C_{23}\alpha_2 + C_{33}\alpha_3) T = \rho \frac{\partial^2 \varphi_z}{\partial t^2} \\
& k_1 \left( \frac{d^2 T}{dr^2} + \frac{1}{r} \frac{dT}{dr} \right) - \frac{k_2}{r^2} b_m^2 T - k_3 b_n^2 T = 0
\end{aligned} \tag{13}$$

Now, the Galerkin finite element method is employed to obtain a solution of the system of Eq. (13) in the radial spatial coordinate. To this end, four field variables  $\varphi_r$ ,  $\varphi_\theta$ ,  $\varphi_z$  and  $T$  are interpolated by considering linear shape functions  $N_i$  and  $N_j$  as

$$\varphi_s = \begin{bmatrix} N_i & N_j \end{bmatrix} \begin{bmatrix} \varphi_{si} \\ \varphi_{sj} \end{bmatrix}, \quad s = r, \theta, z; \quad T = \begin{bmatrix} N_i & N_j \end{bmatrix} \begin{bmatrix} T_i \\ T_j \end{bmatrix} \tag{14}$$

where  $\varphi_{si}$ ,  $\varphi_{sj}$ ,  $T_i$  and  $T_j$  denote the nodal variables.

By substituting Eq. (14) into the first governing equation (13) and applying the Galerkin finite element procedure, one obtains

$$\int_{r_i}^{r_j} \left[ \begin{aligned} & \left[ C_{11} \frac{\partial^2}{\partial r^2} + \frac{C_{11}}{r} \frac{\partial}{\partial r} - \left( \frac{C_{22}}{r^2} + \frac{C_{66}}{r^2} b_m^2 + C_{55} b_n^2 \right) \right] \varphi_r \\ & + \left[ \frac{-b_m (C_{12} + C_{66})}{r} \frac{\partial}{\partial r} + \frac{b_m (C_{22} + C_{66})}{r^2} \right] \varphi_\theta + \left[ -b_n (C_{13} + C_{55}) \frac{\partial}{\partial r} + b_n \frac{(C_{23} - C_{13})}{r} \right] \varphi_z \\ & - (C_{11}\alpha_1 + C_{12}\alpha_2 + C_{13}\alpha_3) \frac{dT}{dr} - \frac{[(C_{11} - C_{12})\alpha_1 + (C_{12} - C_{22})\alpha_2 + (C_{13} - C_{23})\alpha_3]T}{r} - \rho \frac{\partial^2 \varphi_r}{\partial t^2} \end{aligned} \right] N_i dr = 0 \tag{15}$$

After applying integration by part, Eq. (15) reduces to

$$A_1 \varphi_{ri} + B_1 \varphi_{\theta i} + C_1 \varphi_{zi} + D_1 T_i + E_1 \varphi_{rj} + F_1 \varphi_{\theta j} + G_1 \varphi_{zj} + H_1 T_j + I_1 \ddot{\varphi}_{ri} + J_1 \ddot{\varphi}_{rj} = C_{11}^k \frac{\partial \varphi_r}{\partial r} \Big|_i \tag{16}$$

where  $A_1$ ,  $B_1$ , ... and  $J_1$  are constant.

In a similar way, by applying this approach to the second, third and fourth equation (13), three

other differential equations are derived. The mentioned procedure is again repeated by replacing  $N_i$  with  $N_j$  which leads to the four other equations. The result can be written in the dynamic finite element form for each non-boundary element ( $e$ ) as

$$[M]_e \{\ddot{X}\}_e + [K]_e \{X\}_e = \{F\}_e \quad (17)$$

where  $[M]_e$  and  $[K]_e$  are the 8\*8 mass and stiffness matrices and  $\{F\}_e$  is the 8\*1 force vector. Also, the nodal variable vector is defined as

$$\{X\}_e^T = \{\varphi_{r_i} \quad \varphi_{\theta_i} \quad \varphi_{z_i} \quad T_i \quad \varphi_{r_j} \quad \varphi_{\theta_j} \quad \varphi_{z_j} \quad T_j\} \quad (18)$$

By using the inner and outer surface conditions presented in Eq.(10), the displacement and temperature values of the first and last nodes can be obtained in term of the displacement and temperature values of neighboring nodes as

$$\begin{aligned} \varphi_{r_1} &= A_{10}\varphi_{r_2} + B_{10}\varphi_{\theta_2} + C_{10}\varphi_{z_2} + D_{10}T_{in} + E_{10}Q_0(t) \\ \varphi_{\theta_1} &= A'_{10}\varphi_{r_2} + B'_{10}\varphi_{\theta_2} + C'_{10}\varphi_{z_2} + D'_{10}T_{in} + E'_{10}Q_0(t) \\ \varphi_{z_1} &= A''_{10}\varphi_{r_2} + B''_{10}\varphi_{\theta_2} + C''_{10}\varphi_{z_2} + D''_{10}T_{in} + E''_{10}Q_0(t) \\ T_1 &= T_{in} \end{aligned} \quad (19)$$

$$\begin{aligned} \varphi_{r(MI)} &= F_{10}\varphi_{r(MI-1)} + G_{10}\varphi_{\theta(MI-1)} + H_{10}\varphi_{z(MI-1)} + I_{10}T_{out} + J_{10}P_0(t) \\ \varphi_{\theta(MI)} &= F'_{10}\varphi_{r(MI-1)} + G'_{10}\varphi_{\theta(MI-1)} + H'_{10}\varphi_{z(MI-1)} + I'_{10}T_{out} + J'_{10}P_0(t) \\ \varphi_{z(MI)} &= F''_{10}\varphi_{r(MI-1)} + G''_{10}\varphi_{\theta(MI-1)} + H''_{10}\varphi_{z(MI-1)} + I''_{10}T_{out} + J''_{10}P_0(t) \\ T_{MI} &= T_{out} \end{aligned}$$

By substituting Eq. (19) into Eq. (17), the finite element equations of the inner and outer elements are derived as

$$[M]_I \{\ddot{X}\}_I + [K]_I \{X\}_I = \{F\}_I \quad (20)$$

$$[M]_{MI} \{\ddot{X}\}_{MI} + [K]_{MI} \{X\}_{MI} = \{F\}_{MI} \quad (21)$$

For the interfaces, by deriving the continuity conditions (cf. Eq. (9)) between two adjacent layers in terms of displacement and temperature using Eqs. (3), (5), and (6), the displacement and temperature values for two neighboring elements at the interface of  $k$ th and  $k + 1$ th layers (see Fig. 2) can be written as

$$\begin{aligned} \varphi_{r(kI)}^k &= \varphi_{r(kI+1)}^{k+1} = A\varphi_{r(kI-1)}^k + B\varphi_{\theta(kI-1)}^k + C\varphi_{z(kI-1)}^k + DT_{(kI-1)}^k \\ &\quad + E\varphi_{r(kI+2)}^{k+1} + F\varphi_{\theta(kI+2)}^{k+1} + G\varphi_{z(kI+2)}^{k+1} + HT_{(kI+2)}^{k+1} \end{aligned} \quad (22)$$

↓

$$\begin{aligned}
\uparrow \\
\varphi_{\theta(kl)}^k &= \varphi_{\theta(kl+1)}^{k+1} = A' \varphi_{r(kl-1)}^k + B' \varphi_{\theta(kl-1)}^k + C' \varphi_{z(kl-1)}^k + D' T_{(kl-1)}^k \\
&\quad + E' \varphi_{r(kl+2)}^{k+1} + F' \varphi_{\theta(kl+2)}^{k+1} + G' \varphi_{z(kl+2)}^{k+1} + H' T_{(kl+2)}^{k+1} \\
\varphi_{z(kl)}^k &= \varphi_{z(kl+1)}^{k+1} = A'' \varphi_{r(kl-1)}^k + B'' \varphi_{\theta(kl-1)}^k + C'' \varphi_{z(kl-1)}^k + D'' T_{(kl-1)}^k \\
&\quad + E'' \varphi_{r(kl+2)}^{k+1} + F'' \varphi_{\theta(kl+2)}^{k+1} + G'' \varphi_{z(kl+2)}^{k+1} + H'' T_{(kl+2)}^{k+1} \\
T_{(kl)}^k &= T_{(kl+1)}^{k+1} = D''' T_{(kl-1)}^k + H''' T_{(kl+2)}^{k+1}
\end{aligned} \tag{22}$$

where the parameters  $A - H$ ,  $A' - H'$  and  $A'' - H''$  are constant. By substituting the results into Eq. (17), the finite element equation for the last element of the  $k$ th layer and the first element of the  $k + 1$ th layer can be expressed as

$$[M]_k \{\ddot{X}\}_k + [K]_k \{X\}_k = \{F\}_k \tag{23}$$

$$[M]_{k+1} \{\ddot{X}\}_{k+1} + [K]_{k+1} \{X\}_{k+1} = \{F\}_{k+1} \tag{24}$$

Finally, by assembling Eqs. (17), (20), (21), (23), and (24), the general dynamic finite element equation is derived as

$$[M] \{\ddot{X}\} + [K] \{X\} = \{F\} \tag{25}$$

In order to treat the time dependency, the Newmark method (Reddy 1982) is employed. To this goal, the time derivative appeared in the discretized Eq. (25) is approximated by using the implicit time integration scheme of Newmark method with  $\alpha = 0.5$  and  $\beta = 0.25$  (corresponding to the constant average acceleration method).

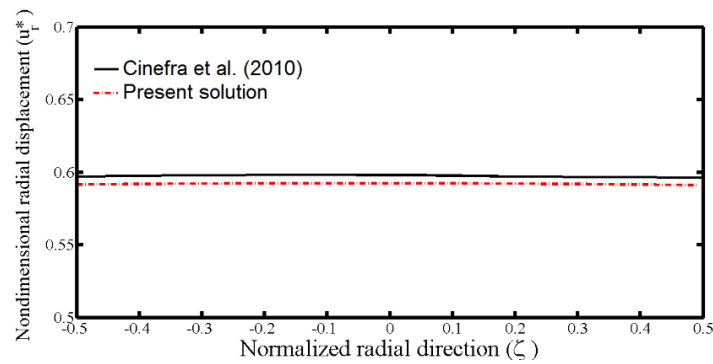
### 3. Numerical results and discussion

In order to examine the accuracy of the present formulations, the results of the static analysis of a conventional metal-ceramic FG cylindrical panel are compared with those available in the open literature. After verification study, benchmark results for the FGS cylindrical panel in thermal environments impacted by pulse loadings are presented and discussed in detail.

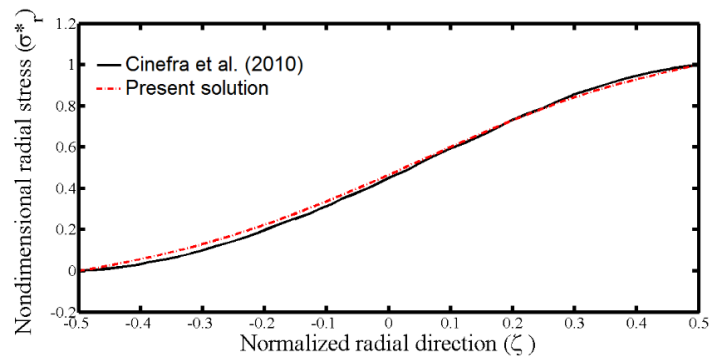
#### 3.1 Verification study

In order to check the validity of the program developed for numerical computations, a simply supported metal-ceramic FG cylindrical panel is analyzed and the results are compared with their counterparts reported by Cinefra *et al.* (2010). The geometric parameters of the panel are  $R_m = 10$ ,  $L = 1$  and  $\theta_m = \pi/3$ . The panel is subjected to the transversely mechanical bi-sinusoidal static loading. The analysis is conducted using Monel (70Ni-30Cu), a nickel-based alloy, as the inner surface metal and Zirconia ( $ZrO_2$ ) as the outer surface ceramic. Material properties gradation through the thickness was assumed to be described with a power law relation (Cinefra *et al.* 2010).

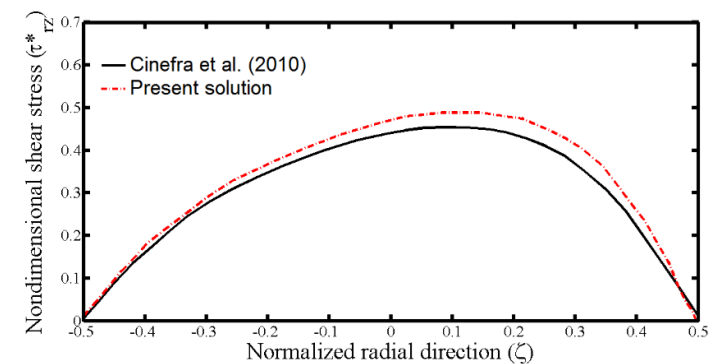
Distribution of nondimensional radial displacement, for the case of  $R_m/h = 100$ , and nondimensional radial/shear stress, for the case of  $R_m/h = 10$ , through the normalized thickness direction ( $\zeta$ ) are plotted in Fig. 3. This figure shows that there is a good correlation between the present results based on 3-D elasticity theory and those obtained for the shell theory so that the maximum discrepancy is mainly less than 3%.



(a)



(b)



(c)

Fig. 3 Through-the-thickness distribution of (a)  $u_r^*$  at  $(\theta = \theta_m/2, z = L/2)$ ; (b)  $\sigma_r^*$  at  $(\theta = \theta_m/2, z = L/2)$ ; and (c)  $\tau_{rz}^*$  at  $(\theta = \theta_m/2, z = L)$  for an FG cylindrical panel

### 3.2 Parametric study

In order to present new results, a cylindrical panel made of functionally gradient steel is considered. Mechanical and thermal loads applied to the inner and outer surfaces of the panel are assumed to be bi-sinusoidal in  $z$  and  $\theta$  directions and defined as

$$\begin{aligned} q_0(\theta, z, t) &= Q_0(t) \sin(b_1\theta) \sin(b_1z) \\ p_0(\theta, z, t) &= P_0(t) \sin(b_1\theta) \sin(b_1z), \quad P_0(t) = 0 \\ T_{in}(\theta, z) &= T_{in} \sin(b_1\theta) \sin(b_1z), \quad T_{in} = 50^\circ C \\ T_{out}(\theta, z) &= T_{out} \sin(b_1\theta) \sin(b_1z), \quad T_{out} = 25^\circ C \end{aligned} \quad (26)$$

Several commonly time-dependent blast loads, as given in Fig. 4, are considered. The definition of the transverse impulsive load  $Q_0(t)$  in the time domain is summarized as

$$(a) \text{ Rectangular pulse: } Q_0(t) = \begin{cases} \bar{Q} & 0 \leq t \leq t_0 \\ 0 & t_0 < t \end{cases} \quad (27a)$$

$$(b) \text{ Half - sine pulse: } Q_0(t) = \begin{cases} \bar{Q} \sin(\pi t/t_0) & 0 \leq t \leq t_0 \\ 0 & t_0 < t \end{cases} \quad (27b)$$

$$(c) \text{ Triangular pulse: } Q_0(t) = \begin{cases} \bar{Q}(1-t/t_0) & 0 \leq t \leq t_0 \\ 0 & t_0 < t \end{cases} \quad (27c)$$

$$(d) \text{ Incremental pulse: } Q_0(t) = \begin{cases} \bar{Q}t/t_0 & 0 \leq t \leq t_0 \\ 0 & t_0 < t \end{cases} \quad (27d)$$

where  $\bar{Q}$  is the magnitude of the imposed blast load and  $t_0$  denotes the loading duration.

The geometry of the panel as shown in Fig. 1 is considered as

$$R_m = 1m, \quad S = \frac{R}{H} = 10, \quad \theta_m = \frac{\pi}{3} \text{ rad}, \quad L = 1m \quad (28)$$

Also, the numerical results in terms of maximum displacements and stresses are presented in dimensionless forms as follows

$$\begin{aligned} (u_r^*, u_\theta^*, u_z^*) &= \frac{100 \max(C_{ij})}{hS^4 \bar{Q}} (u_r, u_\theta, u_z); \\ (\sigma_r^*, \sigma_\theta^*, \sigma_z^*, \tau_{rz}^*, \tau_{r\theta}^*, \tau_{\theta z}^*) &= (\sigma_r, \sigma_\theta, \sigma_z, \tau_{rz}, \tau_{r\theta}, \tau_{\theta z}) / \bar{Q} \end{aligned} \quad (29)$$

It is obvious that the nondimensional quantities do not depend on the load intensity.

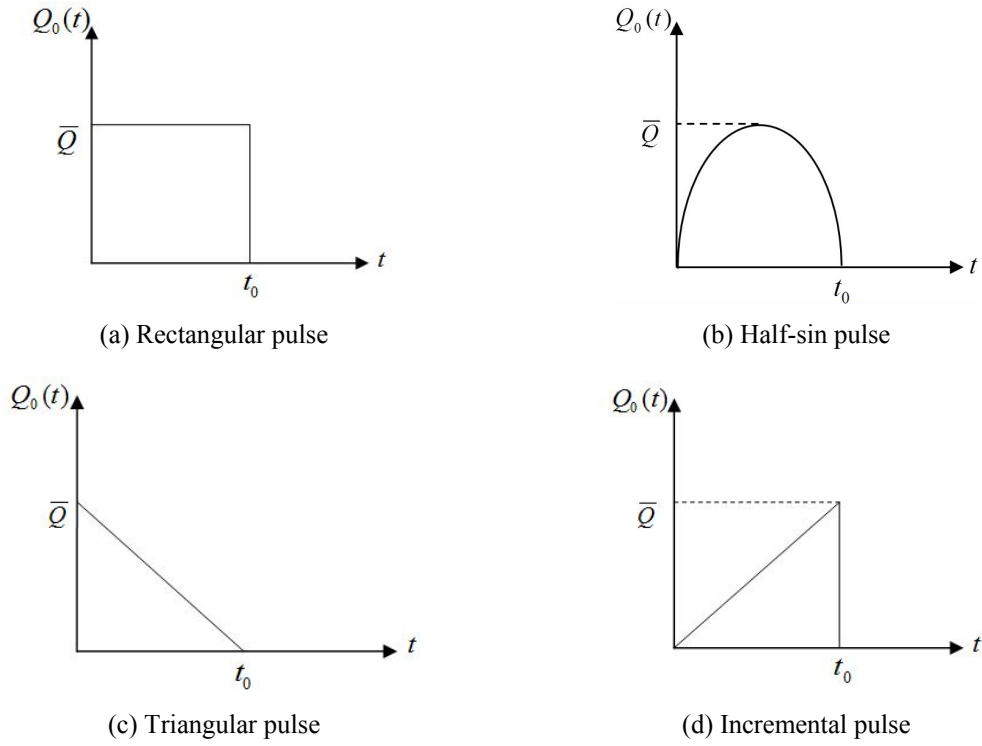


Fig. 4 Load pulse shapes

In the present analysis, three arrangements of FGS composites including  $\alpha\beta\gamma M\gamma$ ,  $\alpha\beta\gamma\beta\alpha$  and  $\gamma\beta\alpha\beta\gamma$  composites are investigated. The thermo-mechanical material properties of  $\alpha\beta\gamma M\gamma$ ,  $\alpha\beta\gamma\beta\alpha$  and  $\gamma\beta\alpha\beta\gamma$  FGS composites such as Young modulus, thermal conductivity coefficient and coefficient of thermal expansion are predicted according to the microhardness profile (Aghazadeh

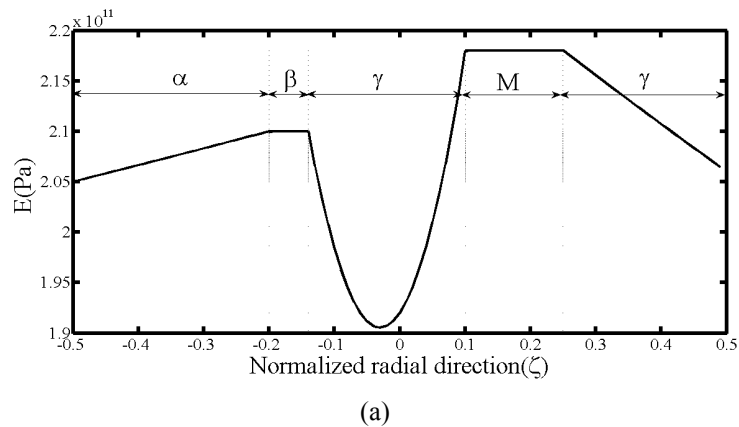
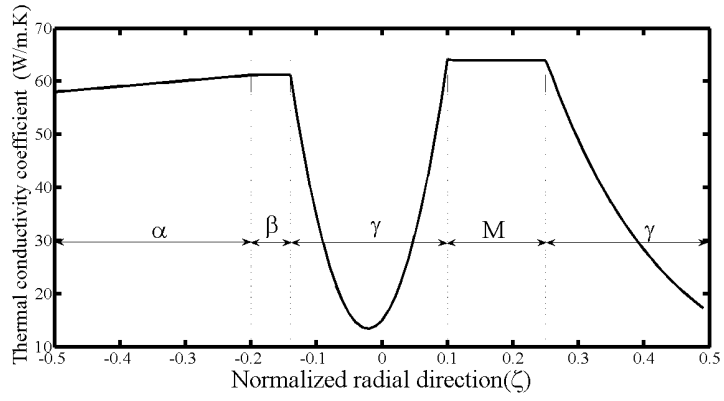
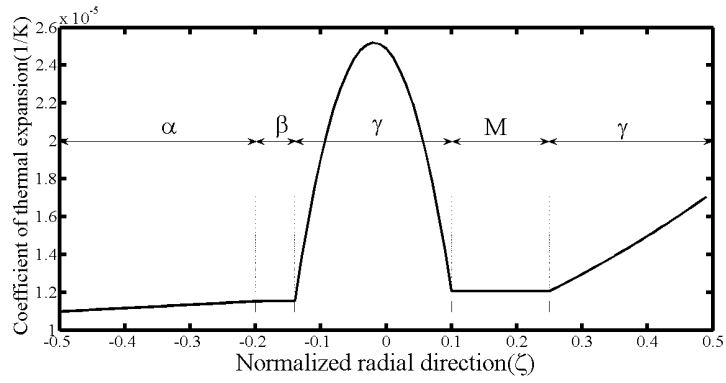


Fig. 5 Distribution of (a) Young modulus; (b) thermal conductivity; and (c) thermal expansion coefficients across the  $\zeta$  in  $\alpha\beta\gamma M\gamma$  FGS composite

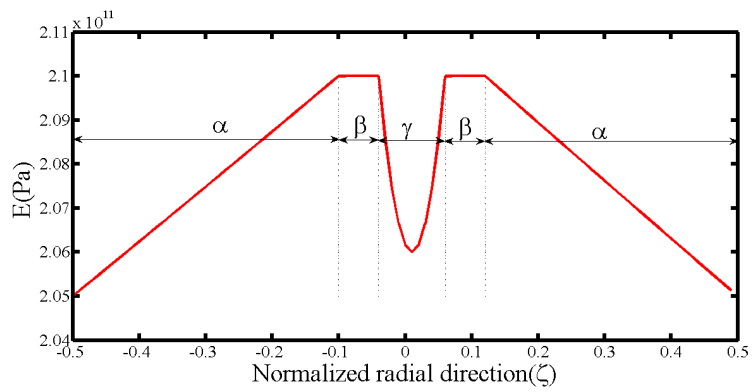


(b)



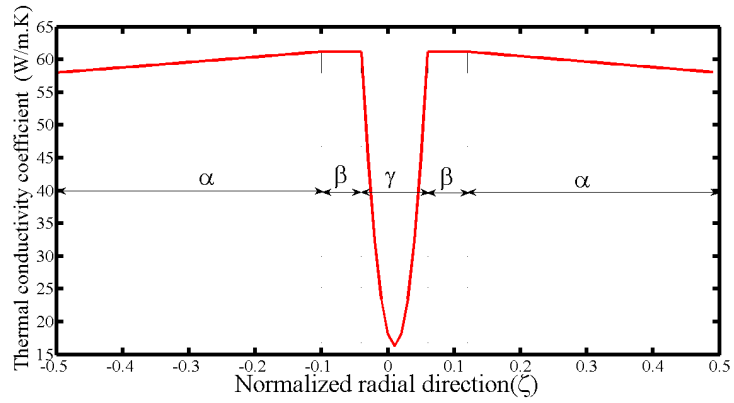
(c)

Fig. 5 Continued

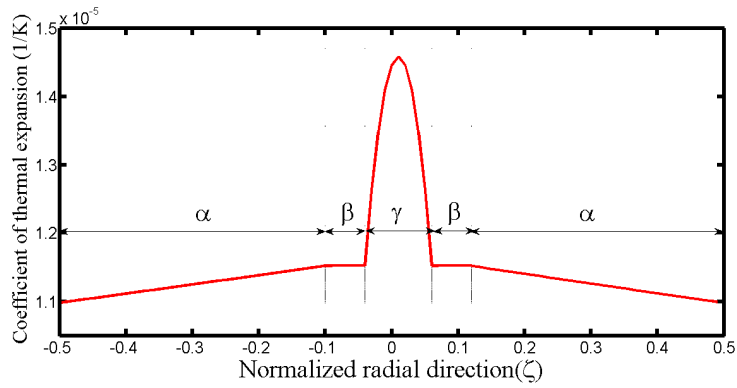


(a)

Fig. 6 Distribution of (a) Young modulus; (b) thermal conductivity; and (c) thermal expansion coefficients across the  $\zeta$  in  $\alpha\beta\gamma\beta\alpha$  FGS composite

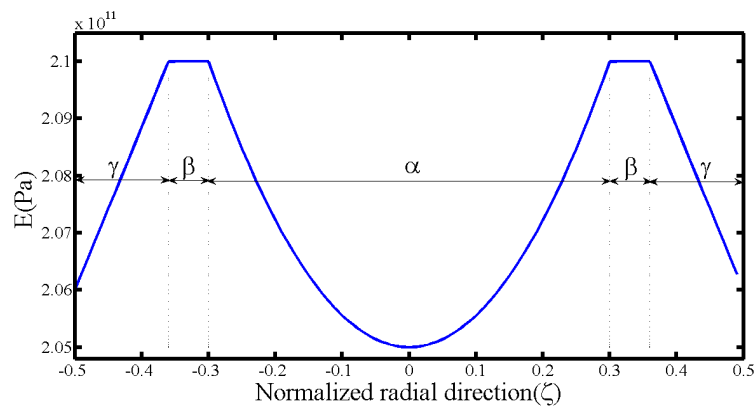


(b)



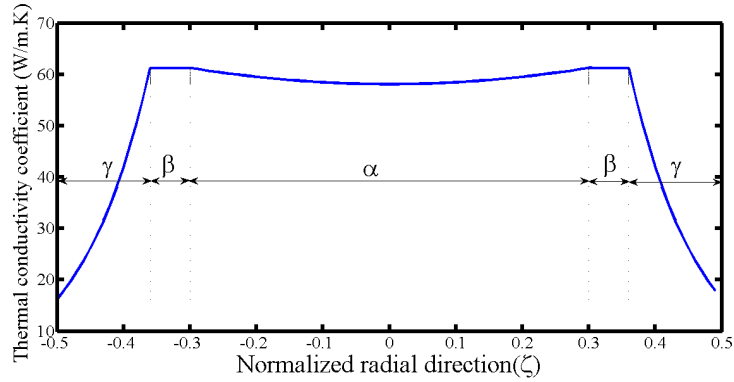
(c)

Fig. 6 Continued

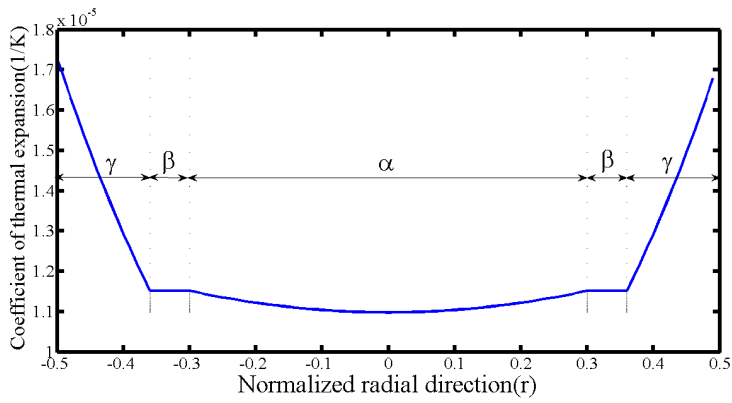


(a)

Fig. 7 Distribution of (a) Young modulus; (b) thermal conductivity; and (c) thermal expansion coefficients across the  $\zeta$  in  $\gamma\beta\alpha\beta\gamma$  FGS composite



(b)



(c)

Fig. 7 Continued

Mohandesi and Shahosseini 2005) and approximated with appropriate functions through Eqs. (1) and (2). The thermo-mechanical material properties through the thickness of FGS cylindrical panel are plotted in Figs. 5 to 7 for  $\alpha\beta\gamma M\gamma$ ,  $\alpha\beta\gamma\beta\alpha$  and  $\gamma\beta\alpha\beta\gamma$  composites, respectively. It is seen that the material properties of  $\alpha\beta\gamma\beta\alpha$  and  $\gamma\beta\alpha\beta\gamma$  composites are symmetric with respect to the middle surface but these parameters are asymmetric for  $\alpha\beta\gamma M\gamma$  composite. Furthermore, as stated before, the values of Poisson ratio and density are assumed to be constant and equal to 0.3 and  $7800 \text{ kg/m}^3$ , respectively.

Numerical results of the dynamic analysis of  $\alpha\beta\gamma M\gamma$ ,  $\alpha\beta\gamma\beta\alpha$  and  $\gamma\beta\alpha\beta\gamma$  FGS cylindrical panels in thermal environments under a rectangular pulse with infinite loading duration ( $t_0 = \infty$ ) are presented in Figs. 8 to 13.

The time histories of the displacement field components,  $u^*_r$ ,  $u^*_\theta$ ,  $u^*_z$ , in the middle surface of the FGS cylindrical panel are depicted in Fig. 8 for the three FGS composites. The presented results in this figure show that all components of the displacement field have the same vibrational period. Also, it is observed that the three FGS composites have a close amplitude of displacements  $u^*_r$  and  $u^*_\theta$ , while  $\alpha\beta\gamma M\gamma$  composite experiences a lower value of axial displacement amplitude with respect to  $\alpha\beta\gamma\beta\alpha$  and  $\gamma\beta\alpha\beta\gamma$  composites.

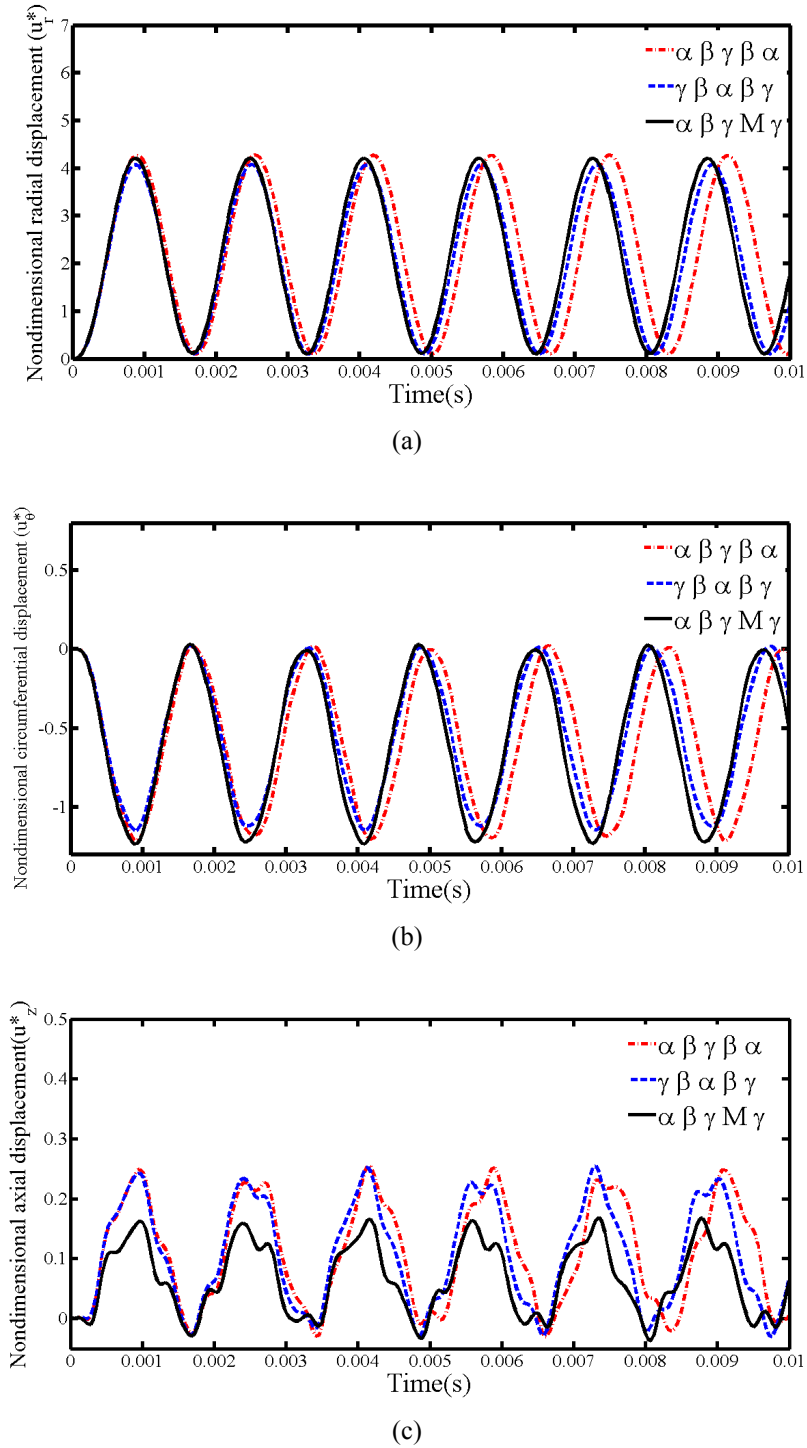
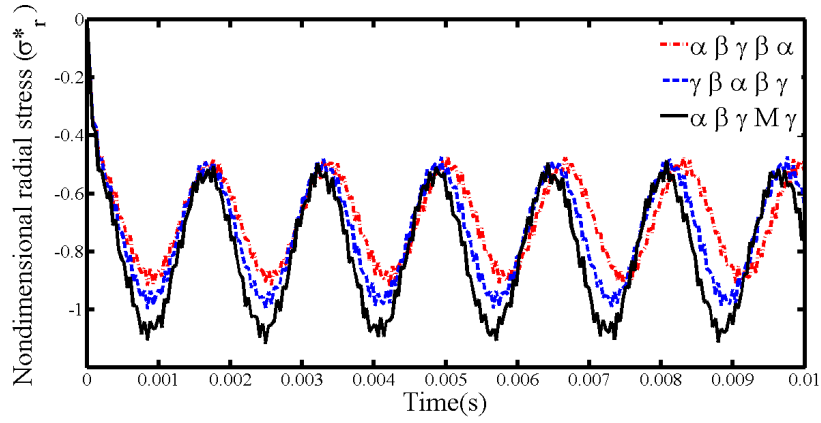
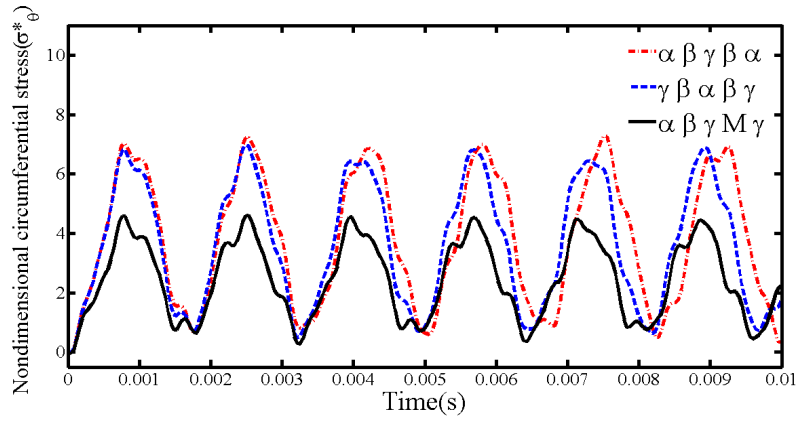


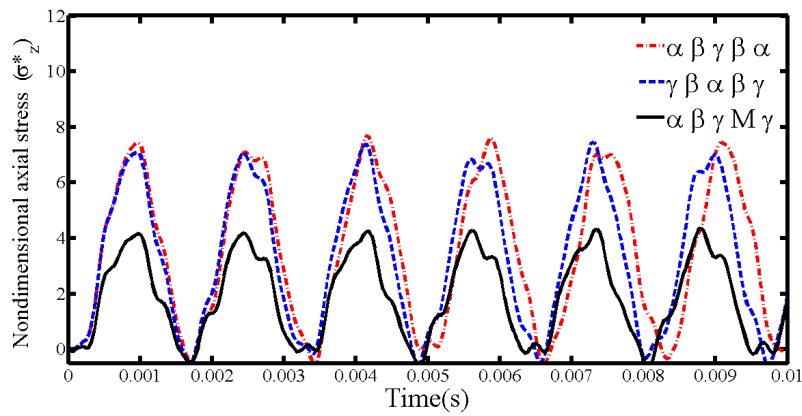
Fig. 8 The time histories of the displacement field components of the FGS cylindrical panel: (a)  $u_r^*$ , at  $(\theta = \theta_m/2, z = L/2, r = R_m)$ ; (b)  $u_\theta^*$  at  $(\theta = \theta_m, z = L/2, r = R_m)$ ; (c)  $u_z^*$  ( $\theta = \theta_m/2, z = L, r = R_m$ )



(a)

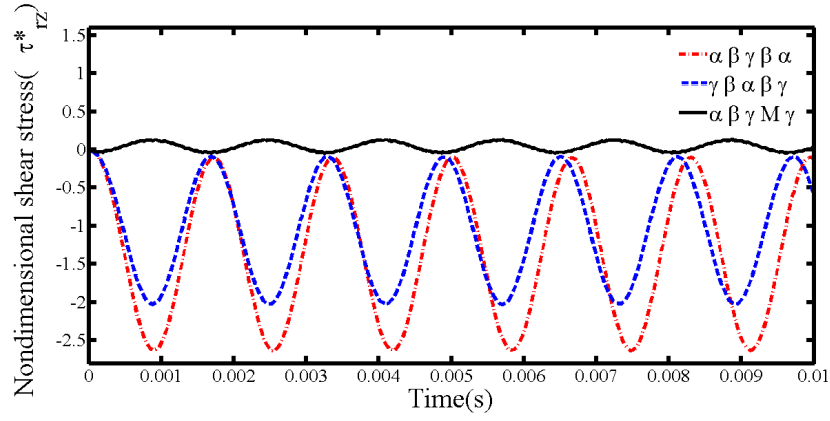


(b)

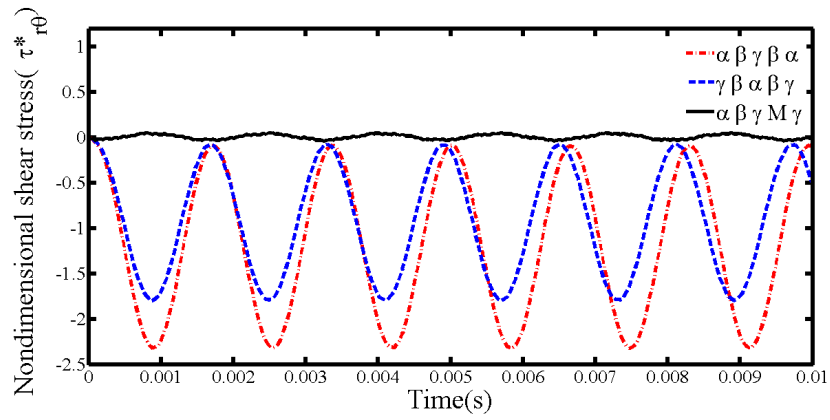


(c)

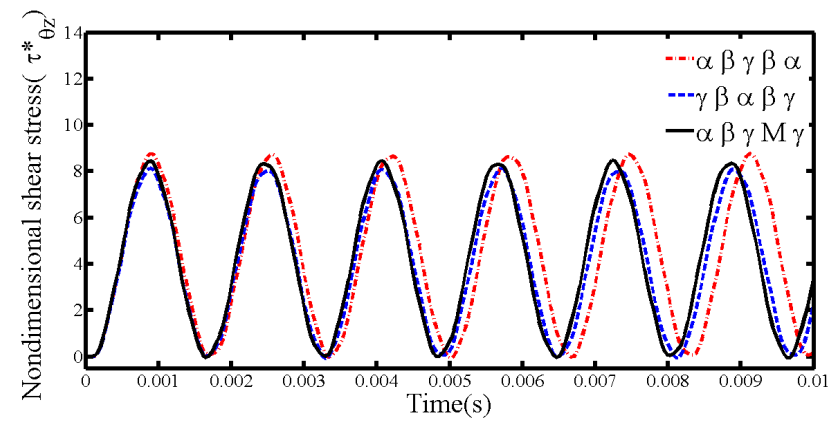
Fig. 9 The time histories of the normal stresses of the FGS cylindrical panel: (a)  $\sigma_r^*$ , at  $(\theta = \theta_m/2, z = L/2, r = R_m)$ ; (b)  $\sigma_\theta^*$  at  $(\theta = \theta_m/2, z = L/2, r = R_m)$ ; (c)  $\sigma_z^*$  at  $(\theta = \theta_m/2, z = L/2, r = R_m)$



(a)



(b)



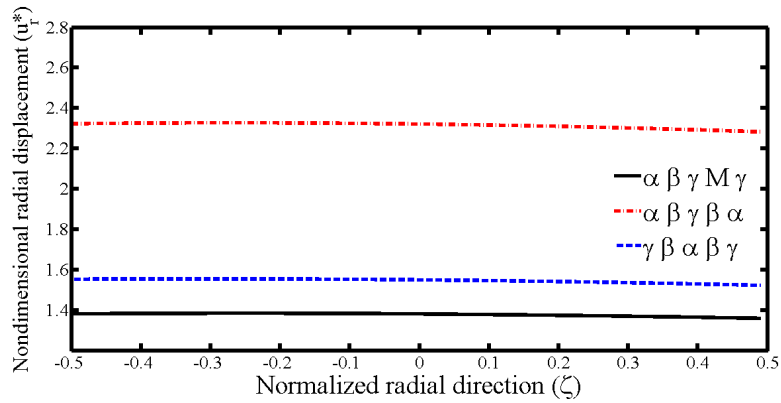
(c)

Fig. 10 The time histories of the shear stresses of the FGS cylindrical panel: (a)  $\tau_{rz}^*$  at  $(\theta = \theta_m/2, z = L, r = R_m)$ ; (b)  $\tau_{r\theta}^*$  at  $(\theta = \theta_m, z = L/2, r = R_m)$ ; (c)  $\tau_{\theta z}^*$  at  $(\theta = \theta_m, z = L, r = R_m)$

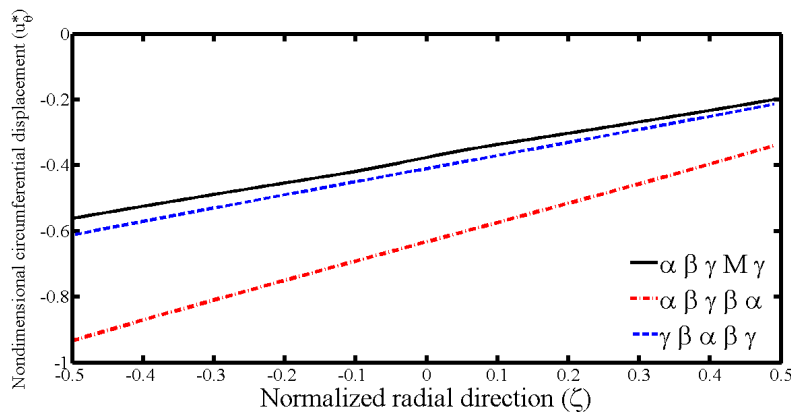
In Fig. 9, the time histories of the normal stresses,  $\sigma_r^*$ ,  $\sigma_\theta^*$ ,  $\sigma_z^*$ , in the middle surface of the FGS cylindrical panel are highlighted. This figure reveals that in-plane normal stresses  $\sigma_\theta^*$  and  $\sigma_z^*$  have a similar trend. It can be seen that  $\alpha\beta\gamma M\gamma$ ,  $\gamma\beta\alpha\beta\gamma$  and  $\alpha\beta\gamma\beta\alpha$  FGS composites result high, intermediate and low levels of the radial stress value, respectively. Also, it is found that the  $\alpha\beta\gamma\beta\alpha$  and  $\gamma\beta\alpha\beta\gamma$  composites have a close amplitude of  $\sigma_\theta^*$  and  $\sigma_z^*$  which are larger than those of  $\alpha\beta\gamma M\gamma$  composite.

The time histories of the shear stresses,  $\tau_{rz}^*$ ,  $\tau_{r\theta}^*$ ,  $\tau_{\theta z}^*$ , in the middle surface of the FGS cylindrical panel are illustrated in Fig. 10. It is seen that out-of-plane shear stresses  $\tau_{rz}^*$  and  $\tau_{r\theta}^*$  have a close trend, as previously found for in-plane normal stresses. Also, it can be concluded that  $\alpha\beta\gamma M\gamma$ ,  $\gamma\beta\alpha\beta\gamma$  and  $\alpha\beta\gamma\beta\alpha$  FGS composites experience low, intermediate and high levels of the out-of-plane shear stresses, respectively. Finally, Fig. 10(c) indicates that the three FGS composites have a close amplitude of the in-plane shear stress  $\tau_{\theta z}^*$ .

Through-the-thickness distribution of displacement and stress fields of FGS cylindrical panels with three different material compositions at  $t = 0.01s$  are illustrated in Figs. 11 to 13. The

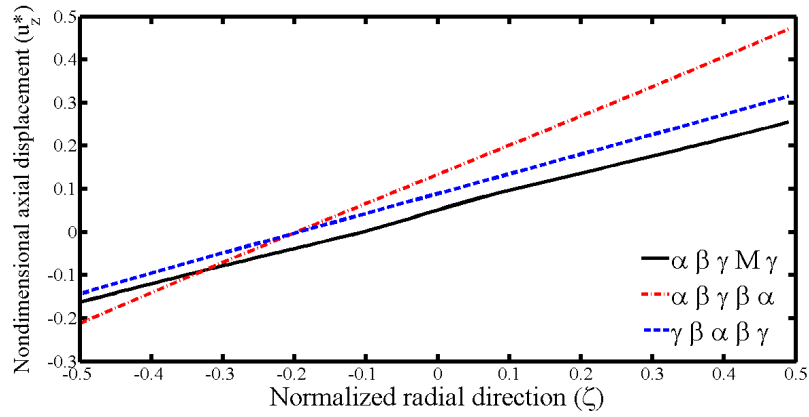


(a)



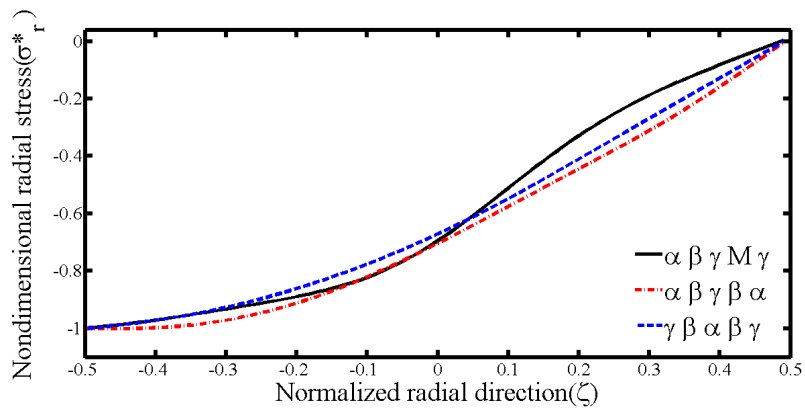
(b)

Fig. 11 Variation of the mechanical displacements of the FGS cylindrical panel versus normalized thickness: (a)  $u_r^*$  at  $(\theta = \theta_m/2, z = L/2)$ ; (b)  $u_\theta^*$  at  $(\theta = \theta_m, z = L/2)$ ; (c)  $u_z^*$  at  $(\theta = \theta_m/2, z = L)$

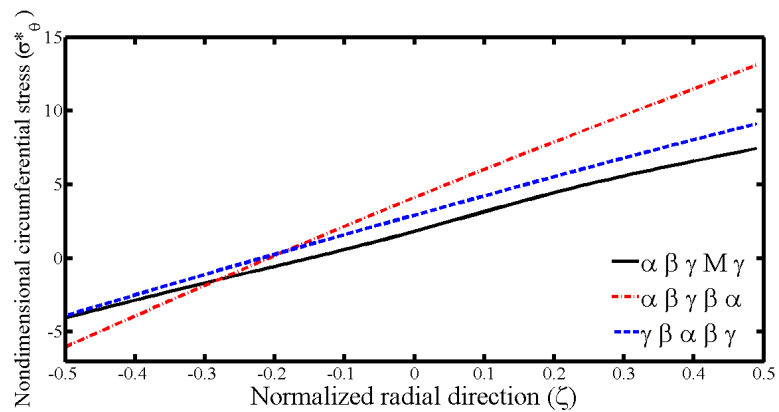


(c)

Fig. 11 Continued

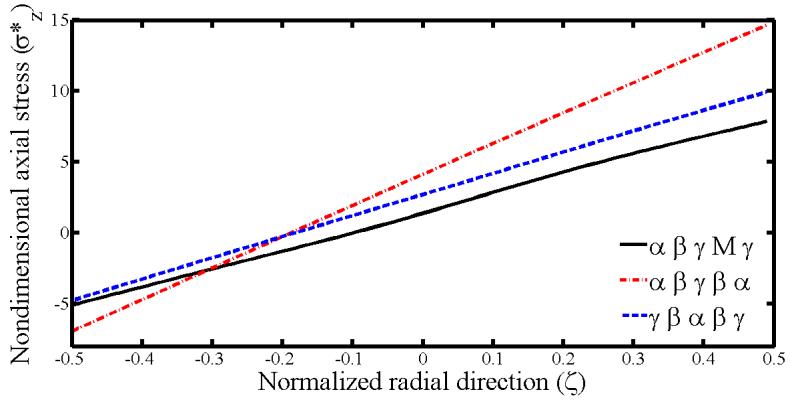


(a)



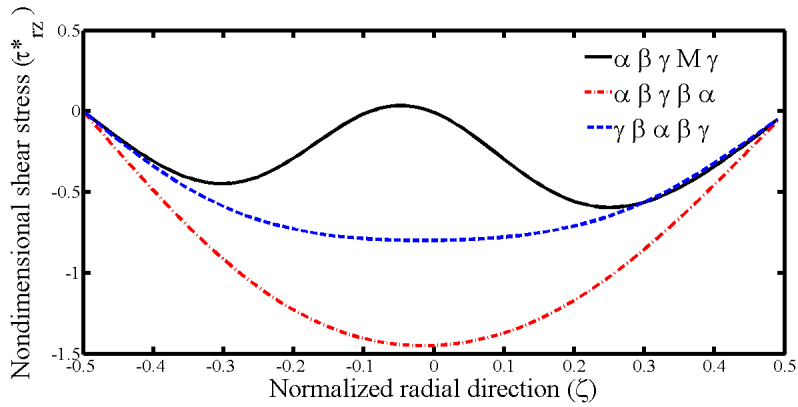
(b)

Fig. 12 Variation of the normal stresses of the FGS cylindrical panel versus normalized thickness: (a)  $\sigma_r^*$  at  $(\theta = \theta_m/2, z = L/2)$ ; (b)  $\sigma_\theta^*$  at  $(\theta = \theta_m/2, z = L/2)$ ; (c)  $\sigma_z^*$  at  $(\theta = \theta_m/2, z = L/2)$

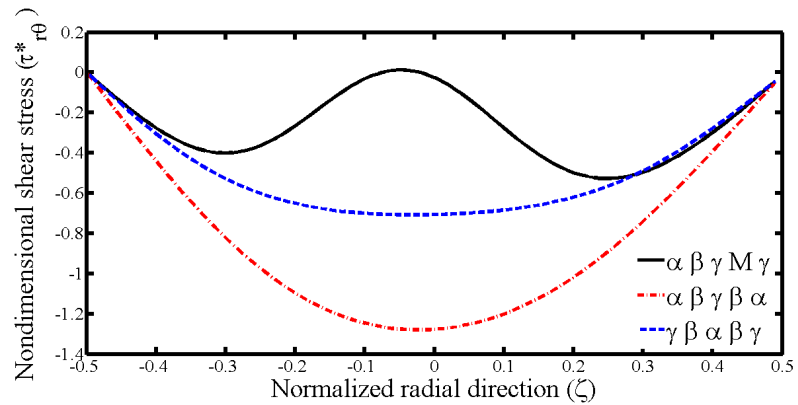


(c)

Fig. 12 Continued



(a)



(b)

Fig. 13 Variation of the shear stresses of the FGS cylindrical panel versus normalized thickness: (a)  $\tau^*_{rz}$  at  $(\theta = \theta_m/2, z = L)$ ; (b)  $\tau^*_{r\theta}$  at  $(\theta = \theta_m, z = L/2)$ , (c)  $\tau^*_{\theta z}$  at  $(\theta = \theta_m, z = L)$

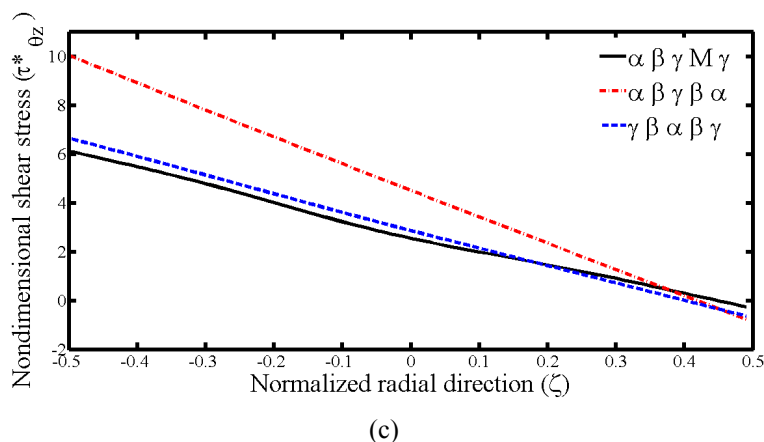


Fig. 13 Continued

preliminary conclusion drawn from these figures is the continuity conditions in interfaces of all adjacent layers and also the mechanical load surface conditions at the inner and outer radiuses are exactly satisfied.

Distribution of the mechanical displacements  $u^*_r$ ,  $u^*_\theta$  and  $u^*_z$  through the thickness of the FGS cylindrical panel is shown in Fig. 11. As can be observed in Fig. 11(a), the radial displacement of the three FGS composites is positive through the whole thickness, since the panel is subjected to the internal pressure. It is seen that the maximum intensity of the radial displacement of  $\alpha\beta\gamma\beta\alpha$  composite is about 1.5 times of that of  $\gamma\beta\alpha\beta\gamma$  composite and is about 1.7 times of that for  $\alpha\beta\gamma M\gamma$  composite. Fig. 11(b) shows that the circumferential displacement of the three composites is negative through the entire thickness of the panel and this value increases from inner radius to outer radius. It is found that the maximum magnitude of the circumferential displacement of  $\alpha\beta\gamma\beta\alpha$  composite (in absolute sense) is about 1.5 times of that of  $\gamma\beta\alpha\beta\gamma$  composite and is about 1.6 times of that for  $\alpha\beta\gamma M\gamma$  composite. The presented results in Fig. 11(c) reveal that the sign of the axial displacement of the three composites changes from negative to positive through the thickness direction. It can be observed that the maximum magnitude of the axial displacement of  $\alpha\beta\gamma\beta\alpha$  composite is about 1.5 times of that of  $\gamma\beta\alpha\beta\gamma$  composite and is about 1.8 times of that for  $\alpha\beta\gamma M\gamma$  composite.

Distribution of the normal stresses  $\sigma^*_r$ ,  $\sigma^*_\theta$  and  $\sigma^*_z$  through the thickness of the FGS panel is illustrated in Fig. 12. This figure shows that the value of the radial stress is negative through the whole thickness of the cylindrical panel. It can be found from Figs. 12(b) and (c) that the circumferential and axial stresses have a similar distribution through the thickness direction, as expected from a geometrical viewpoint. Also, it is seen that these two stresses are compressive on the sections near the inner radius, whereas they are tensile on the sections near the outer radius. Furthermore, it is found that the maximum circumferential and axial stresses occur at the outer radius. Finally, it is observed that the magnitude of the normal stresses (in absolute sense) in  $\alpha\beta\gamma\beta\alpha$  composite is generally more than those of  $\alpha\beta\gamma M\gamma$  and  $\gamma\beta\alpha\beta\gamma$  composites.

Through-the-thickness distribution of the shear stresses  $\tau^*_{rz}$ ,  $\tau^*_{r\theta}$  and  $\tau^*_{\theta z}$  are plotted in Fig. 13. This figure reveals that the shear stresses  $\tau^*_{rz}$  and  $\tau^*_{r\theta}$  are zero on the inner and outer surfaces, as expected. As can be seen in Fig. 13, the shear stresses  $\tau^*_{rz}$  and  $\tau^*_{r\theta}$  have a nearly parabolic

distribution through the thickness direction, while the shear stress  $\tau_{\theta z}^*$  varies almost linearly along the thickness. Figs. 13(a) and (b) show that both  $\alpha\beta\gamma\beta\alpha$  and  $\gamma\beta\alpha\beta\gamma$  composites have a symmetric out-of-plane shear stress distribution through the thickness, whereas  $\alpha\beta\gamma M\gamma$  composite results an asymmetric distribution of out-of-plane shear stress. This is due to the fact that the thermo-mechanical material properties of  $\alpha\beta\gamma\beta\alpha$  and  $\gamma\beta\alpha\beta\gamma$  composites are symmetric with respect to the middle surface but these material parameters are asymmetric for  $\alpha\beta\gamma M\gamma$  composite. It can be found from Figs. 13(a) and (b) that the maximum values of  $\tau_{rz}^*$  and  $\tau_{r\theta}^*$  (in absolute sense) in  $\alpha\beta\gamma\beta\alpha$  and  $\gamma\beta\alpha\beta\gamma$  composites occur around the mean radius, while the maximum out-of-plane shear stress of  $\alpha\beta\gamma M\gamma$  composite takes place at a point between mean radius and the outer radius. Also, it is seen that the values of the shear stresses  $\tau_{rz}^*$  and  $\tau_{r\theta}^*$  in  $\alpha\beta\gamma\beta\alpha$  and  $\gamma\beta\alpha\beta\gamma$  composites are always negative, whereas they become positive for  $\alpha\beta\gamma M\gamma$  composite at the sections near the mean radius. Finally, based on the presented results in Fig. 13, it can be found that  $\alpha\beta\gamma\beta\alpha$  and  $\alpha\beta\gamma M\gamma$  composites experience maximum and minimum shear stresses in absolute sense, respectively. On the other hand, it is seen that the shear stresses of  $\gamma\beta\alpha\beta\gamma$  composite lie between their counterparts related to  $\alpha\beta\gamma\beta\alpha$  and  $\alpha\beta\gamma M\gamma$  composites.

The effect of different time-dependent blast pulses on the time-history of the radial displacement in the middle surface of the FGS cylindrical panel is investigated in Fig. 14 for the three FGS composites. The loading duration is considered to be  $0.005s$ . The presented results in Fig. 14 reveal that the half-sine pulse yields an increasing-decreasing trend of the radial displacement amplitude in the forced motion regime ( $t < t_0$ ). It is seen that among these four pulses,

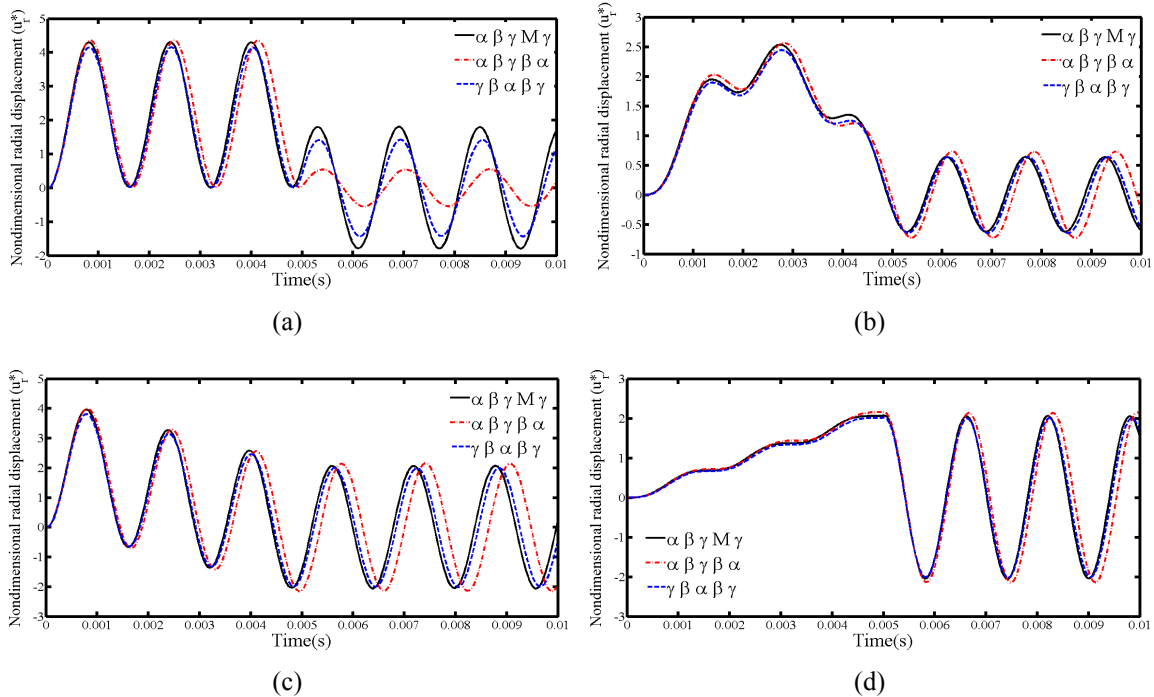


Fig. 14 The time history of the radial displacement  $u_r^*$  of the FGS cylindrical panel subjected to different dynamic pulses: (a) rectangular pulse; (b) half-sin pulse; (c) triangular pulse; (d) incremental pulse at ( $\theta = \theta_m/2$ ,  $z = L/2$ ,  $r = R_m$ )

the incremental pulse results in the least amplitude in the forced motion range. As can be observed from Fig. 14, the three FGS composites have a close amplitude of the radial displacements  $u_r^*$ , in the forced motion regime. However, beyond  $t_0$ , a specific trend for the radial displacement amplitude of the FGS panel with different compositions cannot be determined. By focusing on values of the deflection amplitude of the FGS panel under different blast loads at  $t = t_0 (= 0.005s)$ , it can be found that the oscillation amplitude in the free motion regime ( $t > t_0$ ) extremely depends on the distance from the equilibrium position at the end of forced motion regime. Due to this fact, it is seen that,  $\alpha\beta\gamma\beta\alpha$ ,  $\gamma\beta\alpha\beta\gamma$  and  $\alpha\beta\gamma M\gamma$  FGS composites under rectangular pulse experience respectively low, intermediate and high oscillation amplitudes in the free motion regime. Similarly, it can be found that the radial displacement amplitudes of the three FGS composites under half-sine, triangular and incremental pulses are close to one another in the free vibration range since the values of the deflection related to these three composites are similar at the end of the forced motion regime.

The time history of the shear stress  $\tau_{rz}^*$  in the middle surface of the FGS cylindrical panel are depicted in Fig. 15. It is seen that, in the forced motion regime,  $\alpha\beta\gamma M\gamma$ ,  $\gamma\beta\alpha\beta\gamma$  and  $\alpha\beta\gamma\beta\alpha$  FGS composites undergo vary low, intermediate and high levels of the shear stress, respectively. In a similar way, as stated above for Fig. 14, the shear stress amplitude in the free motion regime depends on the distance from the equilibrium condition at  $t = t_0 = 0.005s$ .

Finally, the effect of loading duration on the dynamic response of the FGS panel under a rectangular pulse is examined in Fig. 16. The results reveal the fact that the distance from the

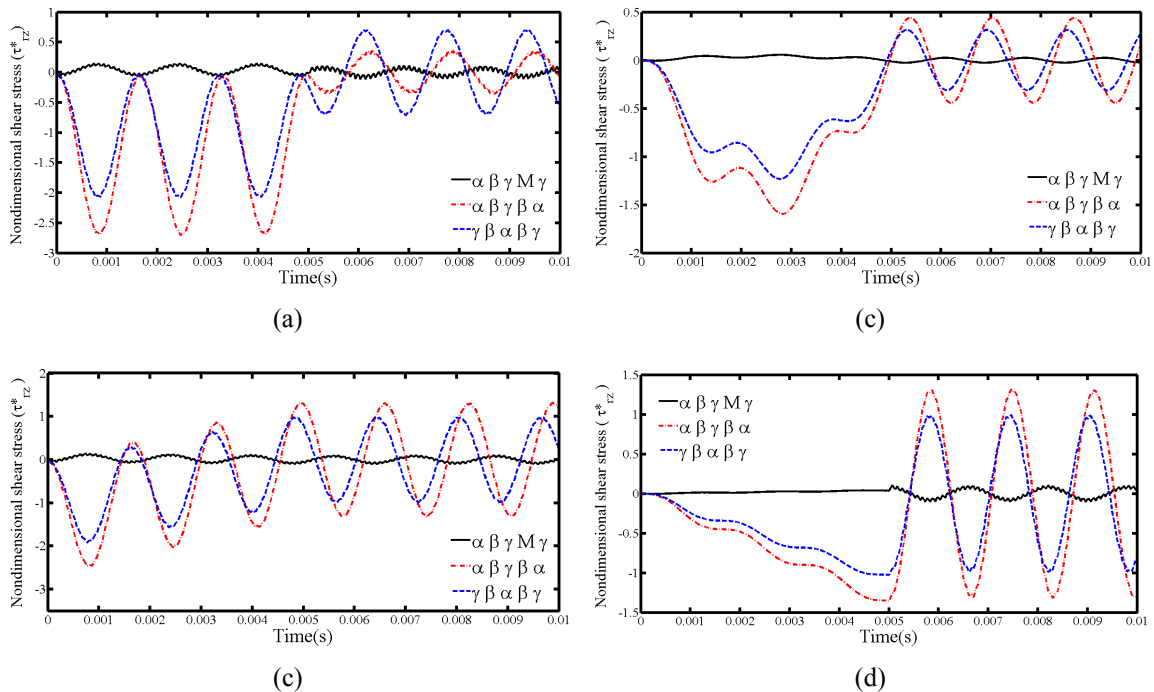


Fig. 15 The time history of the shear stress  $\tau_{rz}^*$  of the FGS cylindrical panel subjected to different dynamic pulses: (a) rectangular pulse; (b) half-sin pulse; (c) triangular pulse; (d) incremental pulse at  $(\theta = \theta_m/2, z = L, r = R_m)$

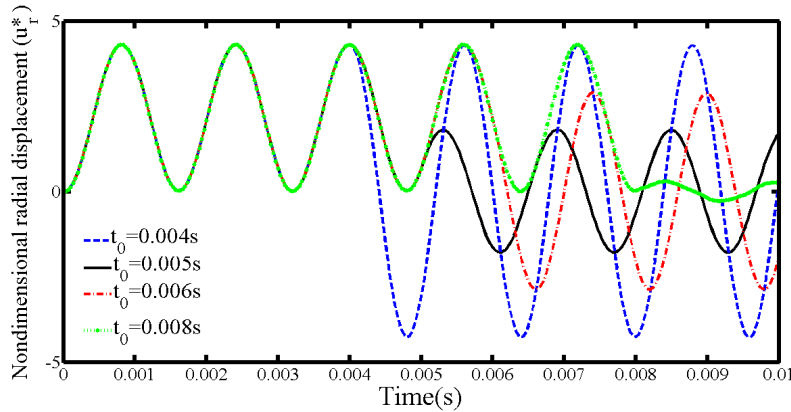


Fig. 16 Influence of loading duration on the radial displacement time history of  $\alpha\beta\gamma M\gamma$  FGS panel subjected to a rectangular pulse at  $(\theta = \theta_m/2, z = L/2, r = R_m)$

equilibrium position at the end of the forced motion range ( $t = t_0$ ) affects the oscillation amplitude in the free motion regime. Fig. 16 shows that the deflection amplitude for  $t_0 = 0.004s$  is significantly higher than the others since the corresponding impulse ends when the amplitude is nearly maximum.

#### 4. Conclusions

In the present work, the dynamic behavior of simply supported functionally gradient steel composite cylindrical panels in thermal environments under impulsive loads was addressed based on the three-dimensional thermo-elasticity theory. Functionally gradient steels containing graded ferritic and austenitic regions together with bainite and martensite intermediate layers were analyzed. Using double Fourier series expansion in the axial and circumferential directions, the governing highly coupled partial differential equations with four independent spatial and time variables reduced to partial differential equations with variable coefficients in radial coordinate and time domains. The resulted partial differential equations were solved by applying the Galerkin finite element method in the radial direction. Finally, the Newmark direct integration method was used to solve algebraic equations in the time domain. In order to verify the present formulations, the results of the static analysis of a conventional metal-ceramic functionally graded panel were compared with existing data in the literature which revealed good agreements. To present novel results, three different arrangements of material compositions of FGSs including  $\alpha\beta\gamma M\gamma$ ,  $\alpha\beta\gamma\beta\alpha$  and  $\gamma\beta\alpha\beta\gamma$  composites were studied. The thermo-mechanical material properties of FGS composites such as the Young modulus, thermal conductivity coefficient and coefficient of thermal expansion were predicted according to the micro hardness profile of FGS composites (Aghazadeh Mohandesi and Shahosseini 2005) and approximated with appropriate functions and plotted through the thickness direction. The presented three-dimensional solution was applied to the transient thermo-elastic analysis of FG austenitic-ferritic cylindrical composite panels subjected to dynamic mechanical and steady-state thermal loadings. Extensive numerical results were presented to provide an insight into the influence of the arrangement of material

compositions of FGSs on the dynamic behavior of FGS cylindrical panels in thermal environments under various impulsive loads.

Due to lack of any data on the dynamic analysis of FGS structures, it is expected that the results supplied in the present work will be instrumental toward a reliable design of FGS structures in thermal environments impacted by pulse loads. The results of present three-dimensional solution are also useful for assessing advanced two-dimensional approximate theories.

## References

- Aghazadeh Mohandesi, J. and Shahosseini, M.H. (2005), "Transformation characteristics of functionally graded steels produced by electroslag remelting", *Metall. Mater. Trans.*, **36**(12), 3471-3476.
- Aghazadeh Mohandesi, J., Shahosseini, M.H. and Parastar Namin, R. (2006), "Tensile behavior of functionally graded steels produced by electroslag remelting", *Metall. Mater. Trans.*, **37**(7), 2125-2132.
- Alibeigloo A., Kani, A.M. and Pashaei, M.H. (2012), "Elasticity solution for the free vibration analysis of functionally graded cylindrical shell bonded to thin piezoelectric layers", *Int. J. Press. Vessel. Pip.*, **89**, 98-111.
- Cinefra, M., Carrera, E., Brischetto, S. and Belouettar, S. (2010) "Thermo-mechanical analysis of functionally graded shells", *J. Therm. Stress.*, **33**(10), 942-963.
- Foroutan, M., Moradi-Dastjerdi, R. and Sotoodeh-Bahreini R. (2011), "Static analysis of FGM cylinders by a mesh-free method", *Steel. Compos. Struct., Int. J.*, **12**(1), 1-11.
- Kamarian, S., Yas, M.H. and Pourasghar, A. (2013), "Free vibration analysis of three-parameter functionally graded material sandwich plates resting on Pasternak foundations", *J. Sandw. Struct. Mater.*, **15**(3), 292-308.
- Nazari, A. and Aghazadeh Mohandesi, J. (2009), "Impact energy of functionally graded steels with crack divider configuration", *J. Mater. Sci. Tech.*, **25**(6), 847-852.
- Nazari, A. and Aghazadeh Mohandesi, J. (2010), "Impact energy of functionally graded steels in crack arrester configuration", *J. Mater. Eng. Perform.*, **19**(7), 1058-1064.
- Reddy, J.N. (1982), "On the solutions to forced motions of rectangular composite plates", *J. Appl. Mech.*, **49**(2), 403-408.
- Santos, H., Mota Soares, C.M., Mota Soares, C.A. and Reddy, J.N. (2009), "A semi-analytical finite element model for the analysis of cylindrical shells made of functionally graded materials", *Compos. Struct.*, **91**(4), 427-432.
- Shen, H.S. (2012), "Nonlinear vibration of shear deformable FGM cylindrical shells surrounded by an elastic medium", *Compos. Struct.*, **94**(3), 1144-1154.
- Sofiyev, A.H. (2010), "Dynamic response of an FGM cylindrical shell under moving loads", *Compos. Struct.*, **93**(1), 58-66.
- Suresh, S. and Mortensen, A. (1998), *Fundamentals of Functionally Graded Materials*, Institute of Materials (IOM) Communications Ltd., London, UK.
- Talebizad, A., Isavand, S., Bodaghi, M., Shakeri, M. and Aghazadeh Mohandesi, J. (2013), "Thermo-mechanical behavior of cylindrical pressure vessels made of functionally graded austenitic/ferritic steels", *Int. J. Mech. Sci.*, **77**, 171-183.
- Zhao, X., Lee, Y.Y. and Liew, K.M. (2009), "Thermoelastic and vibration analysis of functionally graded cylindrical shells", *Int. J. Mech. Sci.*, **51**(9-10), 694-707.